

# Kalman Filter Based Integration of IMU and UWB for High-Accuracy Indoor Positioning and Navigation

Daquan Feng, Chunqi Wang, Chunlong He, Yuan Zhuang, and Xiang-Gen Xia

**Abstract**—The emerging Internet of Things (IoT) applications, such as smart manufacturing and smart home, lead to a huge demand on the provisioning of low-cost and high-accuracy positioning and navigation solutions. Inertial Measurement Unit (IMU) can provide an accurate inertial navigation solution in a short time but its positioning error increases fast with time due to the cumulative error of accelerometer measurement. On the other hand, Ultra-Wideband (UWB) positioning and navigation accuracy will be affected by the actual environment and may lead to uncertain jumps even under Line-of-Sight (LOS) conditions. Therefore, it is hard to use a stand alone positioning and navigation system to achieve high-accuracy in indoor environments. In this paper, we propose an integrated Indoor Positioning System (IPS) combining IMU and UWB through the Extended Kalman Filter (EKF) and Unscented Kalman Filter (UKF) to improve the robustness and accuracy. We also discuss the relationship between the geometric distribution of the base stations (BSs) and the Dilution of Precision (DOP) to reasonably deploy the BSs. The simulation results show that the prior information provided by IMU can significantly suppress the observation error of UWB. It is also shown that the integrated positioning and navigation accuracy of IPS significantly improves that of least squares (LS) algorithm, which only depends on UWB measurements. Moreover, the proposed algorithm has high computational efficiency and can realize real time computation on general embedded devices. In addition, two random motion approximation model algorithms are proposed and evaluated in the real environment. The experimental results show that the two algorithms can achieve certain robustness and continuous tracking ability in the actual IPS.

**Index Terms**—Internet of Things, Inertial Measurement Unit, Ultra-wideband, Indoor Positioning System, Extended Kalman Filter, Unscented Kalman Filter

D. Feng, C. Wang and C. He are with Guangdong Province Engineering Laboratory for Digital Creative Technology and Guangdong Key Laboratory of Intelligent Information Processing, Shenzhen University, 518060, China. C. He is the corresponding author (e-mail: chunlonghe@163.com).

Y. Zhuang is with State Key Laboratory of Information Engineering in Surveying, Mapping and Remote Sensing, Wuhan University, 129 Luoyu Road, Wuhan 430079, China.

X.-G. Xia is with College of Electronics and Information Engineering, Shenzhen University, 518060, China, and also with the Department of Electrical and Computer Engineering, University of Delaware, Newark, DE 19716 USA.

This work was supported in part by the National Natural Science Foundation of China (NSFC) under Grant 61701317, Young Elite Scientists Sponsorship Program by CAST under Grant 2018QNRC001, the Guangdong Natural Science Foundation under Grant 2017A030310371, the Shenzhen Overseas High-level Talents Innovation and Entrepreneurship under Grant KQJSCX20180328093835762, the Tencent Rhinoceros Birds-Scientific Research Foundation for Young Teachers of Shenzhen University, the Natural Science Foundation of SZU, and the Start-up Fund of Peacock Project.

Copyright (c) 2019 IEEE. Personal use of this material is permitted. However, permission to use this material for any other purposes must be obtained from the IEEE by sending a request to pubs-permissions@ieee.org.

## I. INTRODUCTION

LOW-cost and high-accuracy positioning and navigation solutions for indoor mobile robots have become critical in the Internet of Things (IoT) applications, such as smart manufacturing and smart home [1]. Inertial Navigation System (INS) is based on kinematics and Newton classical mechanics [2]. The core of the INS is the Inertial Measurement Unit (IMU), which consists of three-axis accelerometer and three-axis gyroscope [3, 4]. The IMU can obtain the attitude information and motion characteristics of the carrier, such as acceleration, angular velocity and angle [5]. Without using any reference base stations (BSs), the position of the carrier can be directly calculated by mathematical integrations of acceleration. Because of its low-cost, low environmental impact and high-accuracy in a short time period, INS has been widely used in mobile object positioning and navigation scenarios, such as aircrafts, vehicles and pedestrians, but errors increase rapidly with time [6]. On the other hand, many researchers have considered to adopt the Ultra-Wideband (UWB) technology in the Indoor Positioning System (IPS) [7] and lots work has been done including channel model [8], multi-path component estimation [9], and theoretical lower bound of positioning errors [10]. UWB is a communication technology that uses nanosecond non-sinusoidal narrow pulse signal to transmit data, it has become an effective transmission technology in location-aware sensor networks [11]. Inherently, the UWB based ranging technology has the advantages of short pulse interval and high time resolution, and can achieve centimeter-level ranging accuracy [12]. In addition, it has good robustness to against the multi-path effect [13]. However, due to the high frequency band of UWB, it is only suitable for Line-of-Sight (LOS) conditions. When there exists opaque objects, the ranging accuracy will be greatly reduced. Therefore, if only IMU or UWB is used, it is difficult to achieve high-accuracy in complex indoor environments. To this end, researcher has considered to take advantages of their complementary characteristics to improve the positioning and navigation accuracy [14]. A multi-sensor fusion architecture is proposed for the IPS in [15]. When UWB is available and reliable, the long-term drift error of IMU is calibrated by UWB. Otherwise, the system will switch from UWB to IMU immediately to get the positioning and navigation status. In [16], an integrated positioning solution of IMU and UWB is proposed, which can provide reliable and continuous position, especially in the case of Non-Line-of-Sight (NLOS) conditions. However, in [16], to address the time

synchronization issue, all the UWB modules are connected to a central controller via the fiber line. This will increase the complexity of the deployment and the cost of the system. Both [15] and [16] use the time of arrival (TOA) ranging algorithm and have not considered the clock drift effect. Moreover, although the acceleration noise from IMU is considered in the acceleration measurements, the effect of acceleration noise on the velocity and displacement due to the integration is not considered in [15, 16]. In [17], a drift-free and real-time localization and tracking algorithm combining IMU, UWB and region-specific sensor is proposed. It is shown that the fusion algorithm can obtain more accurate three-dimensional velocity and height information by using the lower body biomechanical model. Similarly, a magnetometer-free lower body Motion Capture (MOCAP) algorithm is introduced in [18], where it combines IMU with UWB positioning system and human lower body biomechanical model for three-dimensional positioning and attitude tracking. Note that most of the existing indoor positioning and navigation systems are based on human lower body MOCAP system [19], which increases the cost and deployment difficulty. Moreover, although the drift error in yaw angle estimation can be eliminated by the usage of the magnetometer in [20], it limits the applications under the long-standing magnetic interference in the indoor environment.

Therefore, to achieve low-cost and high-accuracy of the indoor positioning and navigation system, this paper focuses on the integration of IMU and UWB based on Kalman Filter (KF) algorithms. The data obtained by IMU is used for the state equation while the data obtained by UWB is used for the observation equation of KF. In UWB ranging, to better solve the clock synchronization and clock drift problems, we propose an Enhanced Asymmetric Double Sided Two-Way Ranging (EADS-TWR) algorithm. Specifically, in order to further improve the indoor positioning accuracy and reduce the deployment cost of BSs, the Extended Kalman Filter (EKF) algorithm and Unscented Kalman Filter (UKF) algorithm based on three BSs and single BS are adopted in our scheme, respectively. In addition, to reduce the jitter of positioning data, two approximate motion models, namely, Approximate Uniform Motion (AUM) and Approximate Uniform Acceleration Motion (AUAM), are proposed to make the positioning results smoother and more stable. Considering that the positioning accuracy is not only affected by the distance measurement accuracy, but also by the geometric distribution of the BS, we discuss the influence of the geometric distribution of BSs and the Dilution of Precision (DOP) on the positioning accuracy.

The main contributions of this paper can be summarized as follows:

- We propose direct positioning algorithm (DPA) based on EKF fusion for single BS with single distance and angle measurement. Compared with the traditional three BSs least squares (LS) positioning algorithm, the proposed algorithm can greatly reduce the complexity and cost of BS deployment when the positioning accuracy requirement is not high.
- UKF fusion positioning algorithm based on single BS and three BSs are proposed to reduce the computational complexity. The simulation results show that the UKF

fusion algorithm can achieve better positioning accuracy than the EKF fusion positioning algorithm.

- AUAM and AUM approximate motion models are proposed, which can greatly reduce the jitter of positioning data. The experimental results show that the positioning trajectories of the two models are smoother, and the performance of AUM is better than that of AUAM.

In Section II, the basic principles of IPS based on IMU and UWB are described. In Section III, the framework and algorithm of the integrated positioning system based on IMU and UWB are proposed. In Section IV, simulation and experimental results are presented and positioning performances of different algorithms are compared and discussed. In Section V, some conclusions are given.

## II. POSITIONING AND NAVIGATION SYSTEM BASED ON THE INTEGRATION OF IMU AND UWB

In this section, we first describe the architecture of the indoor positioning and navigation system based on the integration of IMU and UWB, and then introduce the IMU based and UWB based positioning algorithms.

Fig.1 describes the architecture of an indoor positioning and navigation system based on the integration of IMU and UWB. The IMU sensor consists of a three-axis accelerometer and a three-axis gyroscope. The UWB sensors consist of an unknown position tag and three BSs with known positions.

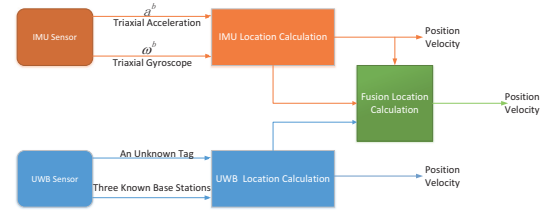


Fig. 1. System architecture of IMU and UWB integration

### A. Positioning processing algorithms based on IMU

A lot of works have been done on the transformations of different coordinate systems and the update calculation of attitude matrix in Strapdown Inertial Navigation System (SINS) [21]. This paper mainly introduces the basic principles, common coordinate systems, and related coordinate transformation matrix theory. The main principle of the SINS is shown in Fig.2.

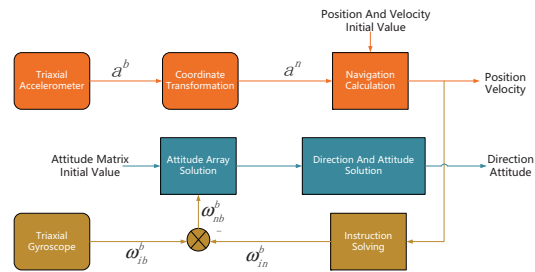


Fig. 2. Principle of strapdown inertial navigation system

To describe the space motion state of the carrier well, it is necessary to choose an appropriate coordinate system. Assume that the body coordinate system (B system) is represented by  $Ox_b y_b z_b$  and the navigation coordinate system (N system) is represented by  $Ox_n y_n z_n$  as shown in Fig.3. The origin coincides with the center of mass of the carrier. In B system, the  $x_b$  axis and  $y_b$  axis point to the front along the longitudinal direction and the right along the transverse direction, respectively, and the  $z_b$  axis is vertical along the carrier and forms the right-hand coordinate system with the  $x_b$  axis and  $y_b$  axis. In N system, the East-North-Down (END) coordinate system is selected. Specifically, the  $x_n$  axis and  $y_n$  axis refer to the East and North directions in the local horizontal plane, respectively, and the  $z_n$  axis points to the down along the vertical line of the earth to form the right-hand system. The coordinate transformation matrix between B system and N system is the attitude matrix of the carrier. The coordinates of the accelerometer and gyroscope in the system belong to B system. The final output of acceleration, velocity and position belong to N system. Note that both Euler angle and quaternion methods can be used for the attitude updating in our IPS. However, considering that Euler angle method is more intuitive and easy to understand than quaternion method, we adopt Euler angle method for the attitude transformation between N system and B system. Taking N system as the reference coordinate system. The heading angle of the carrier is Yaw (expressed in  $\psi$ ), the pitch angle is Pitch (expressed in  $\theta$ ), and the roll angle is Roll (expressed in  $\gamma$ ). The parameters  $\psi$ ,  $\theta$  and  $\gamma$  are a set of Euler angles, which describe the carrier space angular position relationship between N system and B system as shown in Fig.3. When coordinates are rotated with Euler angles, the product of matrices can not be exchanged since different products represent different rotation orders. The transformation matrix is the multiplication of the transformation matrices determined by the basic rotations which will be mathematically shown in details below. The sequence of the multiplication is arranged from right to left in the order of the basic rotations.

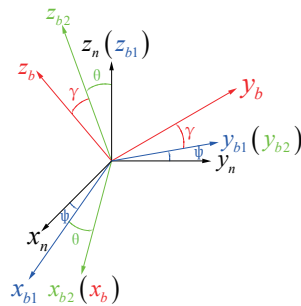


Fig. 3. Determination of carrier space angle position

Let  $C_n^1$ ,  $C_1^2$  and  $C_2^b$  denote the basic rotations from N system to the first rotation system, from the first rotation system to the second rotation system and from the second rotational system to B system, respectively. Then, the coordinate transformation matrix from N system to B system,  $C_n^b$ , can be expressed as follows:

$$C_n^b = C_2^b C_1^2 C_n^1, \quad (1)$$

$$C_2^b = \begin{bmatrix} 1 & 0 & 0 \\ 0 & \cos \gamma & \sin \gamma \\ 0 & -\sin \gamma & \cos \gamma \end{bmatrix}, \quad (2)$$

$$C_1^2 = \begin{bmatrix} \cos \theta & 0 & -\sin \theta \\ 0 & 1 & 0 \\ \sin \theta & 0 & \cos \theta \end{bmatrix}, \quad (3)$$

$$C_n^1 = \begin{bmatrix} \cos \psi & \sin \psi & 0 \\ -\sin \psi & \cos \psi & 0 \\ 0 & 0 & 1 \end{bmatrix}. \quad (4)$$

On the other hand, the transformation matrix between two Cartesian coordinate systems is an orthogonal matrix. Thus,

$$C_b^n = (C_n^b)^{-1} = (C_n^b)^T, \quad (5)$$

$$C_b^n = \begin{bmatrix} \cos \psi \cos \theta & C_{12} & C_{13} \\ \cos \theta \sin \psi & C_{22} & C_{23} \\ -\sin \theta & \sin \gamma \cos \theta & \cos \theta \cos \gamma \end{bmatrix}, \quad (6)$$

where  $C_b^n$  is the coordinate transformation matrix from B system to N system and

$$C_{12} = \sin \gamma \sin \theta \cos \psi - \cos \gamma \sin \psi,$$

$$C_{13} = \sin \gamma \sin \psi + \cos \gamma \sin \theta \cos \psi,$$

$$C_{22} = \cos \psi \sin \gamma + \sin \gamma \sin \theta \sin \psi,$$

$$C_{23} = \sin \psi \sin \theta \cos \gamma - \sin \gamma \cos \psi.$$

In the system, attitude updating refers to the real-time calculation of matrix  $C_b^n$  based on the output of IMU. Let  $\omega_{nb}$  denote the angular velocity of B system relative to N system. Then, the components of  $\omega_{nb}$  in B system,  $\omega_{nb}^b$ , can be given as follows:

$$\begin{bmatrix} \omega_{nbx}^b \\ \omega_{nby}^b \\ \omega_{nbz}^b \end{bmatrix} = C_2^b C_1^2 \begin{bmatrix} 0 \\ 0 \\ -\psi \end{bmatrix} + C_2^b \begin{bmatrix} 0 \\ \theta \\ 0 \end{bmatrix} + \begin{bmatrix} \gamma \\ 0 \\ 0 \end{bmatrix}. \quad (7)$$

Then, by expanding and merging, the Euler angle differential equation can be obtained as follows:

$$\begin{bmatrix} \dot{\gamma} \\ \dot{\theta} \\ \dot{\psi} \end{bmatrix} = \begin{bmatrix} 1 & 0 & -\sin \theta \\ 0 & \cos \gamma & \sin \gamma \cos \theta \\ 0 & -\sin \gamma & \cos \gamma \cos \theta \end{bmatrix}^{-1} \begin{bmatrix} \omega_{nbx}^b \\ \omega_{nby}^b \\ \omega_{nbz}^b \end{bmatrix}. \quad (8)$$

The acceleration in B system,  $a^b$ , is measured by the three-axis accelerometer:

$$a^b = [a_x^b \ a_y^b \ a_z^b]^T. \quad (9)$$

Thus, the acceleration in N system,  $a^{n1}$ , can be obtained by the coordinate transformation:

$$a^{n1} = [a_x^{n1} \ a_y^{n1} \ a_z^{n1}]^T = C_b^n a^b, \quad (10)$$

If the gravity vector,  $g$ , is removed from the acceleration of N system, then the acceleration in N system,  $a^n$ , is obtained:

$$a^n = \begin{bmatrix} a_x^{n1} \\ a_y^{n1} \\ a_z^{n1} \end{bmatrix} = \begin{bmatrix} a_x^{n1} \\ a_y^{n1} \\ a_z^{n1} \end{bmatrix} - \begin{bmatrix} 0 \\ 0 \\ g \end{bmatrix}. \quad (11)$$

When the sample interval is short, the carrier is approximately subjected to constant force and with uniform acceleration of linear motion. Let  $\Delta v^n$  denote the velocity variation

in N system. Then, by substituting Newton's second law for momentum conservation equation, we have

$$\begin{bmatrix} \Delta v_x^n \\ \Delta v_y^n \\ \Delta v_z^n \end{bmatrix} = \begin{bmatrix} a_x^n \\ a_y^n \\ a_z^n \end{bmatrix} \Delta t. \quad (12)$$

Let  $v^n(t)$  denote the velocity in N system at time  $t$ . Then, the velocity in N system at time  $t+1$ ,  $v^n(t+1)$ , can be obtained by the acceleration integral as follows:

$$\begin{bmatrix} v_x^n(t+1) \\ v_y^n(t+1) \\ v_z^n(t+1) \end{bmatrix} = \begin{bmatrix} v_x^n(t) \\ v_y^n(t) \\ v_z^n(t) \end{bmatrix} + \begin{bmatrix} \Delta v_x^n \\ \Delta v_y^n \\ \Delta v_z^n \end{bmatrix}. \quad (13)$$

Let  $\Delta \chi^n$  denote the displacement variation in N system. Then,

$$\begin{bmatrix} \Delta \chi_x^n \\ \Delta \chi_y^n \\ \Delta \chi_z^n \end{bmatrix} = \begin{bmatrix} v_x^n \\ v_y^n \\ v_z^n \end{bmatrix} \Delta t + \frac{1}{2} \begin{bmatrix} a_x^n \\ a_y^n \\ a_z^n \end{bmatrix} \Delta t^2. \quad (14)$$

Let  $\chi^n(t)$  denote the position in N system at time  $t$ , and then the position in N system at time  $t+1$ ,  $\chi^n(t+1)$ , can be described as follows:

$$\begin{bmatrix} \chi_x^n(t+1) \\ \chi_y^n(t+1) \\ \chi_z^n(t+1) \end{bmatrix} = \begin{bmatrix} \chi_x^n(t) \\ \chi_y^n(t) \\ \chi_z^n(t) \end{bmatrix} + \begin{bmatrix} \Delta \chi_x^n \\ \Delta \chi_y^n \\ \Delta \chi_z^n \end{bmatrix}. \quad (15)$$

### B. Positioning processing algorithm based on UWB

The wireless signal based positioning methods are generally divided into the ranging-based and non-ranging-based methods. The UWB positioning method usually adopts the ranging-based algorithm and has two steps. The first step is to measure the distance and angle information, and the second step is to calculate the position using the measurement distance and angle information.

Time of Flight (TOF) ranging is the common method to measure the distance between two nodes. Most existing works in TOF adopt the Symmetric Double Sided Two-Way Ranging (SDS-TWR) technology [22] and as shown in Fig.4(a) to mitigate the influence of clock synchronization between nodes. However, the frequency drift caused by the crystal clock drift can not be solved. Besides, SDS-TWR technology requires a long processing time [23]. To overcome the above problems, we propose an improved EADS-TWR optimization algorithm in our model as shown in Fig.4(b).

Define  $T_{\text{prop}}$  as the time of flight between device A and device B,  $T_{\text{roundA}}$  as the time duration from device A sending the polling message to receiving the response message from device B,  $T_{\text{roundB}}$  as the time from device B sending the response message to receiving the final message from device A, and  $T_{\text{replyA}}$  and  $T_{\text{replyB}}$  as the time delay of devices A and B, respectively. Then, according to Fig.4(b), it is easy to see that  $T_{\text{roundA}}$  and  $T_{\text{roundB}}$  can be expressed as follows:

$$\begin{aligned} T_{\text{roundA}} &= 2T_{\text{prop}} + T_{\text{replyB}}, \\ T_{\text{roundB}} &= 2T_{\text{prop}} + T_{\text{replyA}}. \end{aligned} \quad (16)$$

Thus, we can get the time of flight between device A and B as below:

$$T_{\text{prop}} = \frac{T_{\text{roundA}} \times T_{\text{roundB}} - T_{\text{replyA}} \times T_{\text{replyB}}}{T_{\text{roundA}} + T_{\text{roundB}} + T_{\text{replyA}} + T_{\text{replyB}}}. \quad (17)$$

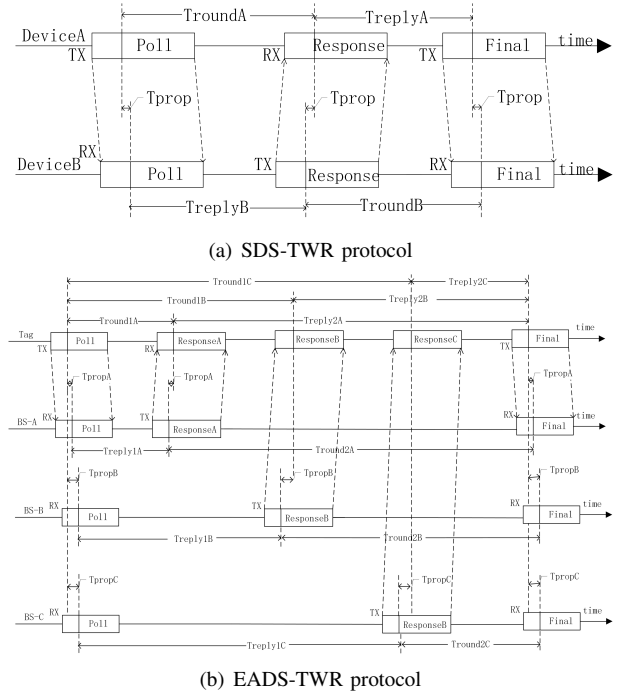


Fig. 4. Double sided two way ranging protocol

Then, the distance,  $d$ , can be expressed as:

$$d = cT_{\text{prop}}, \quad (18)$$

where  $c$  is the propagation velocity of electromagnetic wave.

After completing the ranging process, we adopt the multi-lateration to determine the position of the tag based on the distance measurements. Specifically, Fig.5 shows an example of trilateration, where the distances from the tag to three BSs are measured. Obviously, in the two-dimensional plane, the tag should be located at the intersection of three circles centered on three BSs. As long as the three BSs are not in a straight line, the result of the trilateration is unique.

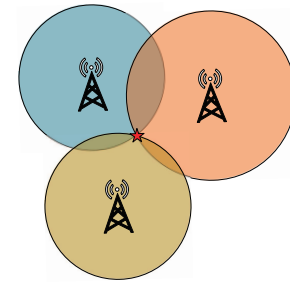


Fig. 5. Least square (LS) position algorithm of three BSs

Assuming that the unknown tag is located at  $(x, y)$  and the  $i^{\text{th}}$  BS is located at  $(x_i, y_i)$ . Then, the true distance between the unknown tag and the  $i^{\text{th}}$  BS,  $d_i$ , can be expressed as below:

$$d_i = \sqrt{(x_i - x)^2 + (y_i - y)^2}. \quad (19)$$

Let  $d'_i$  denote the measured distance between the unknown tag and the  $i^{\text{th}}$  BS. Then, the difference between the true distance and the measured distance can be expressed as  $\rho_i = d_i - d'_i$ . To

deal with the ranging noise, we adopt the classic LS method to minimize the value of  $\sum_{i=1}^n \rho_i^2$ . Specifically, each distance determines an equation for the position of an unknown tag:

$$\begin{cases} d_1^2 = (x_1 - x)^2 + (y_1 - y)^2 \\ d_2^2 = (x_2 - x)^2 + (y_2 - y)^2 \\ \vdots \\ d_n^2 = (x_n - x)^2 + (y_n - y)^2 \end{cases} \quad (20)$$

Let all the equations subtract the first equation, we can get

$$A\varepsilon = b, \quad (21)$$

where

$$A = \begin{bmatrix} x_2 - x_1 & y_2 - y_1 \\ x_3 - x_1 & y_3 - y_1 \\ \vdots & \vdots \\ x_n - x_1 & y_n - y_1 \end{bmatrix}, \quad \varepsilon = \begin{bmatrix} x \\ y \end{bmatrix}, \quad (22)$$

$$b = \frac{1}{2} \begin{bmatrix} x_2^2 + y_2^2 - d_2^2 - (x_1^2 + y_1^2 - d_1^2) \\ x_3^2 + y_3^2 - d_3^2 - (x_1^2 + y_1^2 - d_1^2) \\ \vdots \\ x_n^2 + y_n^2 - d_n^2 - (x_1^2 + y_1^2 - d_1^2) \end{bmatrix},$$

Thus, the LS solution of  $\varepsilon$  is

$$\varepsilon = (A^T A)^{-1} A^T b. \quad (23)$$

In the LS method, each ranging value has adopted the same weight. Obviously, in the process of ranging, when the carrier is closer to the BS, the ranging error is smaller. Therefore, we choose a larger weight for the smaller ranging value, the positioning accuracy will be further improved. To this end, we propose the Weighted Least Squares (WLS) algorithm to solve the problem, in which the weighting coefficient,  $\eta$ , is expressed by the reciprocal of the ranging value,  $d$  as

$$\eta = \begin{bmatrix} \frac{1}{d_2} & 0 & 0 & 0 \\ 0 & \frac{1}{d_3} & 0 & 0 \\ 0 & 0 & \ddots & 0 \\ 0 & 0 & 0 & \frac{1}{d_n} \end{bmatrix}. \quad (24)$$

Then, the WLS solution of  $\hat{\varepsilon}$  is expressed as

$$\hat{\varepsilon} = (A^T \eta A)^{-1} A^T \eta b. \quad (25)$$

### III. MULTI-SENSOR DATA FUSION ALGORITHM BASED ON IMU AND UWB

In this section, we first introduce the EKF fusion positioning algorithm according to three distance measurements. Then, we propose the UKF fusion positioning algorithm by only single distance and angle measurements. Finally, we develop two approximate motion models, namely, AUM and AUAM, to further reduce the jitter of positioning data.

In the SINS, the positioning error may increase rapidly with time due to the cumulative error of accelerometer measurement [24]. On the other hand, UWB can provide centimeter-level ranging and positioning accuracy. However, UWB signal is vulnerable to the obstacles and only suitable for LOS conditions. To this end, we consider to improve the positioning

accuracy of the carrier by using Kalman filter to merge the data from IMU and UWB sensors.

It is known that linear Kalman filter can derive the optimal carrier state under the condition of linear Gaussian model, in which the noises of IMU and UWB sensors are independent with each other and both obey Gaussian distribution with zero mean and variances  $\sigma^2$ . However, there always exist some degrees of nonlinearity in the actual system, such as the square relation and trigonometric function relation in state equation or observation equation. To more accurately approximate the nonlinear systems, various filtering algorithms are adopted to deal with the nonlinear factors. In [25], a dual filter integration for Micro-Electro-Mechanical Systems (MEMS) sensors and WiFi fingerprints are proposed, where the EKF algorithm is used to obtain the smooth constrained fingerprints.

#### A. EKF algorithm based on distance measurements

In the two-dimensional plane, assume that the tag is moving in a straight line with uniform acceleration, define  $\hat{X}(k)$  as the state vector at time  $k$ , contains position,  $x(k)$ , velocity,  $v(k)$ , and acceleration,  $a(k)$ , which can be expressed as follows:

$$X(k) = [x_x(k) \quad x_y(k) \quad v_x(k) \quad v_y(k) \quad a_x(k) \quad a_y(k)]^T. \quad (26)$$

When the sample time period is  $T$ ,  $T\omega(k)$  denotes the process noise of acceleration,  $\frac{T^2}{2}\omega(k)$  denotes the process noise of velocity and  $\frac{T^3}{6}\omega(k)$  denotes the process noise of position due to the double integral of acceleration, according to the equation of uniform acceleration motion at time  $k+1$ . Thus, the state equation can be expressed as follows:

$$\begin{cases} x_x(k+1) = x_x(k) + v_x(k)T + \frac{1}{2}a_x(k)T^2 + \frac{T^3}{6}\omega_x(k) \\ x_y(k+1) = x_y(k) + v_y(k)T + \frac{1}{2}a_y(k)T^2 + \frac{T^3}{6}\omega_y(k) \\ v_x(k+1) = v_x(k) + a_x(k)T + \frac{T^2}{2}\omega_x(k) \\ v_y(k+1) = v_y(k) + a_y(k)T + \frac{T^2}{2}\omega_y(k) \\ a_x(k+1) = a_x(k) + T\omega_x(k) \\ a_y(k+1) = a_y(k) + T\omega_y(k) \end{cases} \quad (27)$$

Then, the state equation in matrix form is expressed as follows:

$$X(k+1) = FX(k) + GW(k), \quad (28)$$

where  $F$  denotes the state transition matrix,  $G$  denotes the noise driving matrix,  $W(k) = [\omega_x(k) \quad \omega_y(k)]^T$  denotes process noise vector with zero mean and covariance matrix  $Q = \text{diag}(\sigma_{ax}^2, \sigma_{ay}^2)$  at time  $k$ .

$$F = \begin{bmatrix} 1 & 0 & T & 0 & \frac{T^2}{2} & 0 \\ 0 & 1 & 0 & T & 0 & \frac{T^2}{2} \\ 0 & 0 & 1 & 0 & T & 0 \\ 0 & 0 & 0 & 1 & 0 & T \\ 0 & 0 & 0 & 0 & 1 & 0 \\ 0 & 0 & 0 & 0 & 0 & 1 \end{bmatrix}, \quad G = \begin{bmatrix} \frac{T^3}{6} & 0 \\ 0 & \frac{T^3}{6} \\ \frac{T^2}{2} & 0 \\ 0 & \frac{T^2}{2} \\ T & 0 \\ 0 & T \end{bmatrix}. \quad (29)$$

Let  $Z(k)$  denote the observation vector, containing the true distance  $d_i(k)$  with the observation noise  $v_i(k)$  at time  $k$ .





$v_d(k)$  and observation angle noise  $v_\varphi(k)$  at time  $k$ . Then, the observation equation can be expressed as follows:

$$Z_u(k) = \begin{bmatrix} d(k) + v_d(k) \\ \varphi(k) + v_\varphi(k) \end{bmatrix} = h(X(k)) + V_u(k), \quad (34)$$

where  $h(X(k))$  is a non-linear function of the observation equation, and  $V_u(k) = [v_d(k) \ v_\varphi(k)]^T$  is the observation noise vector with zero mean and covariance matrix  $R_u = \text{diag}(\sigma_d^2, \sigma_\varphi^2)$ .

$$\begin{bmatrix} d(k) \\ \varphi(k) \end{bmatrix} = \begin{bmatrix} \sqrt{(x_x(k) - x_0)^2 + (x_y(k) - y_0)^2} \\ \arctan\left(\frac{x_y(k) - y_0}{x_x(k) - x_0}\right) \end{bmatrix}. \quad (35)$$

Unlike EKF, UKF does not need to compute the Jacobian matrix at each time and adopts UT to make the statistics keep consistent for the random variables undergoing nonlinear transformation [27]. For the Gaussian distribution, through carefully selecting the sample points, UT can capture the mean and covariance accurately to the third-order. The selection of sample points is based on the prior mean and covariance matrix. Define a non-linear transformation  $y = f(x)$ , where the random variable  $x$  is  $n$ -dimensional with mean  $\bar{x}$  and covariance matrix  $P$ . Then, the statistical characteristics of  $y$  can be calculated by forming a matrix  $\chi$  of  $2n+1$  sigma points  $\chi^{(i)}$  with the corresponding weight  $\omega$  as follows:

$$\begin{cases} \chi^{(0)} = \bar{x}, \\ \chi^{(i)} = \bar{x} + \left(\sqrt{(n+\lambda)P}\right)_i, i = 1, \dots, n, \\ \chi^{(i)} = \bar{x} - \left(\sqrt{(n+\lambda)P}\right)_i, i = n+1, \dots, 2n, \end{cases} \quad (36)$$

where  $(\sqrt{P})_i$  represents the  $i^{\text{th}}$  column of the square root of a matrix. The corresponding weights of these sample points are calculated as follows:

$$\begin{cases} \omega_m^{(0)} = \frac{\lambda}{n+\lambda}, \\ \omega_c^{(0)} = \frac{\lambda}{n+\lambda} + (1 - \alpha^2 + \beta), \\ \omega_m^{(i)} = \omega_c^{(i)} = \frac{1}{2(n+\lambda)}, i = 1, 2, \dots, 2n, \end{cases} \quad (37)$$

where  $\omega_m^{(i)}$  is the weight of mean and  $\omega_c^{(i)}$  is the weight of covariance of the sigma points, the superscript  $i$  is the index of sample points,  $\lambda \triangleq \alpha^2(n + \kappa) - n$  is a scaling parameter to reduce the total prediction error. In practical,  $\alpha$  is usually set to a small positive value to keep the mean of the sigma points around  $\bar{x}$ ,  $\kappa$  is set to zero to ensure that the matrix  $(n + \lambda)P$  is a semi-positive definite matrix, and  $\beta$  is a non-negative weight coefficient to incorporate the prior distribution of  $x$ . According to Eq.(36) and Eq.(37), we can get a set of sigma points  $X_u^{(i)}(k|k)$ , and then further predict them to get the state mean and state covariance matrix as  $\bar{X}_u(k+1|k)$  and  $P_u(k+1|k)$ , respectively. Similarly, we can get the observation mean and observation covariance matrix as  $\bar{Z}_u(k+1|k)$  and  $P_{z_k z_k}$ , respectively, and also the cross covariance matrix as  $P_{x_k z_k}$  between the state vector and the observation vector. Then, we can calculate the Kalman gain,  $K$ , and finally obtain the state and state covariance matrix updates as  $X_u(k+1|k+1)$  and  $P_u(k+1|k+1)$ , respectively. The detailed process of UKF algorithm is shown in Algorithm 2.

#### Algorithm 2 Unscented Kalman Filter Algorithm

**Initialize:** State mean  $U_u(0) = E[X_u(0)]$ , state covariance matrix  $P_u(0) = \text{var}[X_u(0)]$ .

1: Calculate sigma points.

$$X_u^{(i)}(k|k) = \begin{bmatrix} \bar{X}_u(k|k) \\ \bar{X}_u(k|k) + \sqrt{(n+\lambda)P_u(k|k)} \\ \bar{X}_u(k|k) - \sqrt{(n+\lambda)P_u(k|k)} \end{bmatrix}^T,$$

2: Predict sigma points.

$$\hat{X}_u^{(i)}(k+1|k) = F X_u^{(i)}(k|k), i = 1, \dots, 2n+1,$$

3: Calculate state mean and state covariance matrix.

$$\begin{aligned} \bar{X}_u(k+1|k) &= \sum_{i=0}^{2n} \omega_m^{(i)} \hat{X}_u^{(i)}(k+1|k), \\ P_u(k+1|k) &= \sum_{i=0}^{2n} \omega_c^{(i)} \left[ \hat{X}_u^{(i)}(k+1|k) - \bar{X}_u(k+1|k) \right] \\ &\quad \left[ \hat{X}_u^{(i)}(k+1|k) - \bar{X}_u(k+1|k) \right]^T + Q_u, \end{aligned}$$

4: Update sigma points.

$$X_u^{(i)}(k+1|k) = \begin{bmatrix} \bar{X}_u(k+1|k) \\ \bar{X}_u(k+1|k) + \sqrt{(n+\lambda)P_u(k+1|k)} \\ \bar{X}_u(k+1|k) - \sqrt{(n+\lambda)P_u(k+1|k)} \end{bmatrix}^T,$$

5: Predict observation.

$$\hat{Z}_u^{(i)}(k+1|k) = h\left(X_u^{(i)}(k+1|k)\right), i = 1, \dots, 2n+1,$$

6: Calculate observation mean and observation covariance matrix.

$$\begin{aligned} \bar{Z}_u(k+1|k) &= \sum_{i=0}^{2n} \omega_m^{(i)} \hat{Z}_u^{(i)}(k+1|k), \\ P_{z_k z_k} &= \sum_{i=0}^{2n} \omega_c^{(i)} \left[ \hat{Z}_u^{(i)}(k+1|k) - \bar{Z}_u(k+1|k) \right] \\ &\quad \left[ \hat{Z}_u^{(i)}(k+1|k) - \bar{Z}_u(k+1|k) \right]^T + R_u, \\ P_{x_k z_k} &= \sum_{i=0}^{2n} \omega_c^{(i)} \left[ \hat{X}_u^{(i)}(k+1|k) - \bar{X}_u(k+1|k) \right] \\ &\quad \left[ \hat{Z}_u^{(i)}(k+1|k) - \bar{Z}_u(k+1|k) \right]^T, \end{aligned}$$

7: Calculate Kalman gain matrix.

$$K = P_{x_k z_k} P_{z_k z_k}^{-1},$$

8: Update state and state covariance matrix.

$$\begin{aligned} X_u(k+1|k+1) &= \bar{X}_u(k+1|k) + K [Z_u(k+1) - \bar{Z}_u(k+1|k)], \\ P_u(k+1|k+1) &= P_u(k+1|k) - K P_{z_k z_k} K^T. \end{aligned}$$

### C. Dilution of precision models

The positioning accuracy is not only affected by the distance measurement accuracy, but also by the geometric distribution of the BS. The DOP represents the geometric distribution of tag and BSs, which plays an important role in the positioning accuracy. The DOP mainly includes the following parameters: geometric dilution of precision (GDOP), position dilution of precision (PDOP), horizontal dilution of precision (HDOP), vertical dilution of precision (VDOP) and time dilution of precision (TDOP). This paper focuses on the positioning of the tag in the two-dimensional plane. Under the same distance measurement accuracy, the smaller the HDOP, the higher the positioning accuracy. Therefore, it is important to arrange the BS distribution reasonably to reduce the HDOP value. In detail, the HDOP can be defined as:

$$HDOP = \frac{\sqrt{\sigma_x^2 + \sigma_y^2}}{\sigma_d}, \quad (38)$$

where  $\sigma_d$  is the standard deviation of distance measurement error,  $\sigma_x^2$  and  $\sigma_y^2$  are the variances of  $x$  axis and  $y$  axis, respectively. According to Eq.(19), the derivatives at the approximate position  $(x', y')$  can be given as follows:

$$\begin{bmatrix} d_1 - d'_1 \\ d_2 - d'_2 \\ \vdots \\ d_n - d'_n \end{bmatrix} = \begin{bmatrix} \frac{\partial d_1}{\partial x} & \frac{\partial d_1}{\partial y} \\ \frac{\partial d_2}{\partial x} & \frac{\partial d_2}{\partial y} \\ \vdots & \vdots \\ \frac{\partial d_n}{\partial x} & \frac{\partial d_n}{\partial y} \end{bmatrix} \begin{bmatrix} x - x' \\ y - y' \end{bmatrix}, \quad (39)$$

where

$$\begin{cases} \frac{\partial d_i}{\partial x} = \frac{x_i - x'}{\sqrt{(x_i - x')^2 + (y_i - y')^2}}, \\ \frac{\partial d_i}{\partial y} = \frac{y_i - y'}{\sqrt{(x_i - x')^2 + (y_i - y')^2}}. \end{cases}$$

When  $n \geq 3$ , the LS method can be used to solve Eq.(39) and we can get

$$C = (B^T B)^{-1} B^T D, \quad (40)$$

where

$$D = \begin{bmatrix} d_1 - d'_1 \\ d_2 - d'_2 \\ \vdots \\ d_n - d'_n \end{bmatrix}, B = \begin{bmatrix} \frac{\partial d_1}{\partial x} & \frac{\partial d_1}{\partial y} \\ \frac{\partial d_2}{\partial x} & \frac{\partial d_2}{\partial y} \\ \vdots & \vdots \\ \frac{\partial d_n}{\partial x} & \frac{\partial d_n}{\partial y} \end{bmatrix}, C = \begin{bmatrix} x - x' \\ y - y' \end{bmatrix}.$$

The covariance matrix of distance error,  $R$ , is the same as that in the EKF algorithm. The positioning error covariance matrix,  $Q_c$ , caused by distance error can be expressed as follows:

$$\begin{aligned} Q_c &= (B^T R^{-1} B)^{-1} B^T R^{-1} \sigma_u^2 \\ &= (B^T B)^{-1} \sigma_u^2, \\ &= E \sigma_u^2 \end{aligned} \quad (41)$$

where  $E = (B^T B)^{-1}$  is a symmetric matrix representing the influence of distance error on positioning error,  $\sigma_u^2$  is the variance of user equivalent ranging error (UERE), the smaller UERE means better positioning accuracy [28]. Let

$$E = \begin{bmatrix} E_{11} & E_{12} \\ E_{21} & E_{22} \end{bmatrix}. \quad (42)$$

Finally, we can get the  $HDOP = \sqrt{E_{11} + E_{22}}$ .

### D. AUAM and AUM approximate motion models

Since the motion of the tag is usually random, it is difficult to establish an accurate motion model. Therefore, we propose two approximate motion models in a short time period: one is the AUAM model and the other is AUM model. Specifically, the AUAM model combines the position and the differential velocity information from the UWB as well as the acceleration information from the IMU. The whole procedure of the AUAM filtering algorithm is shown in Algorithm 3. Without considering the acceleration from the IMU sensor, the AUAM model will degenerate into the AUM model which only integrates the position and differential velocity information.

#### Algorithm 3 AUAM Filtering Algorithm

**Initialize:**UWB sample time period  $t=0.02s$  (the rate of updates by the UWB is 50Hz), IMU sample time period  $T=0.01s$  (the rate of updates by the IMU is 100Hz)

- 1: Measure the distance.

$$d = [d_1 \quad d_2 \quad \dots \quad d_n]$$

- 2: Calculate the LS position.

$$\varepsilon(k) = (A^T A)^{-1} A^T b$$

- 3: Calculate the differential velocity.

$$v(k) = \frac{\varepsilon(k) - \varepsilon(k-1)}{t}$$

- 4: Convert the acceleration coordinate system.

$$a^n = [a_x^n \quad a_y^n] = C_b^n a^b$$

- 5: Update the position state.

$$\varepsilon(k+1) = \varepsilon(k) + v(k)t + \frac{1}{2}a^n T^2$$

## IV. SIMULATION AND EXPERIMENTAL RESULTS

In this section, we evaluate the performance of the proposed algorithm by simulation and experiment. Firstly, we compare the EKF fusion positioning algorithm with the LS and WLS positioning algorithms. Then, we evaluate the performances of the UKF fusion algorithm and the DPA algorithm based on single BS. In addition, we compare the performances of the proposed EKF and UKF algorithms. Finally, we carry out experiments in the laboratory to verify the actual effect of the proposed algorithms.

### A. EKF simulation results

In the simulations, it is assumed that the tag moves in the  $xy$  plane with the initial position at (0,0), the initial horizontal and vertical velocities are both at 0.15m/s, the initial horizontal and vertical accelerations are both at 0.002m/s<sup>2</sup>, the sample time period  $T=1s$ , and the total running time  $N=50s$ .

Fig.7 demonstrates the performances of the LS and the proposed EKF algorithms in terms of the positioning trajectory and error, where  $Q$  and  $R$  denote the process and observation noise variances, respectively. As shown in Fig.7(a), the LS



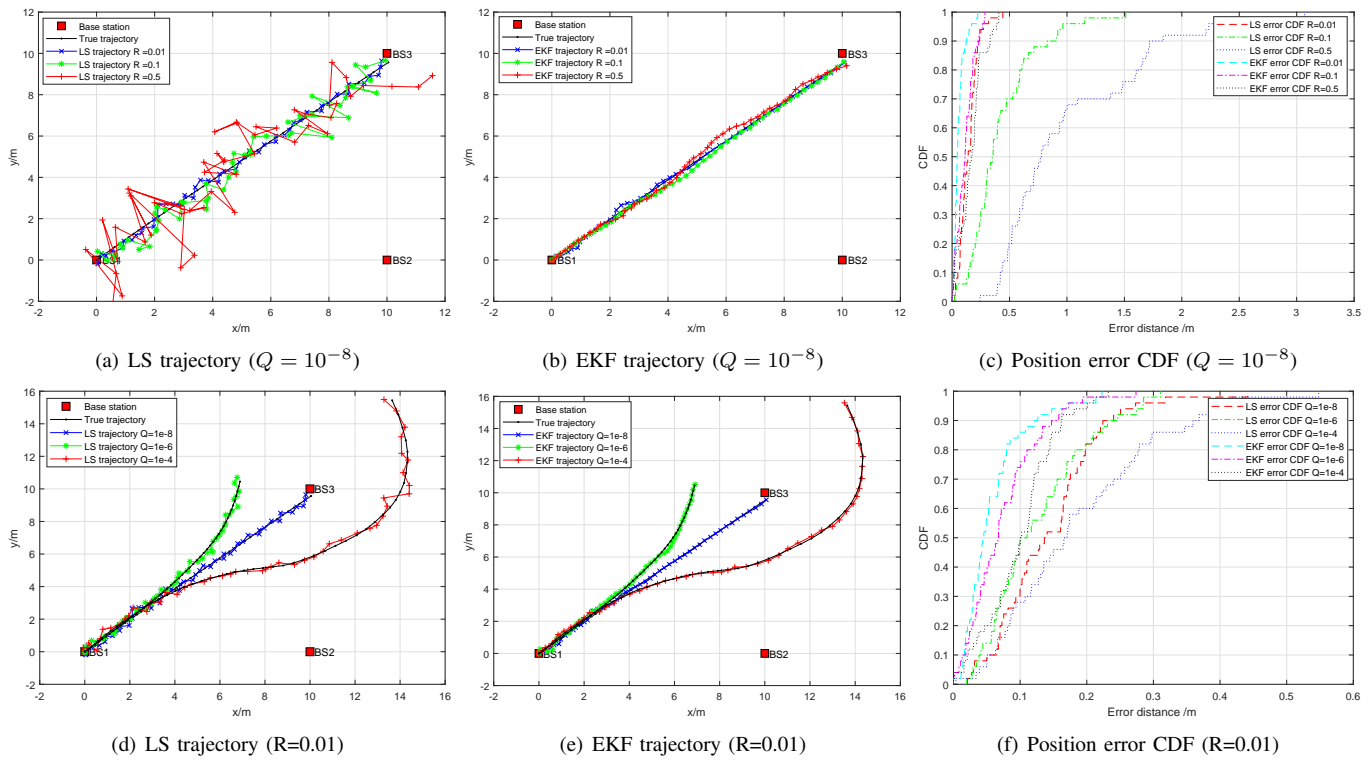


Fig. 7. The performances of LS and EKF algorithms

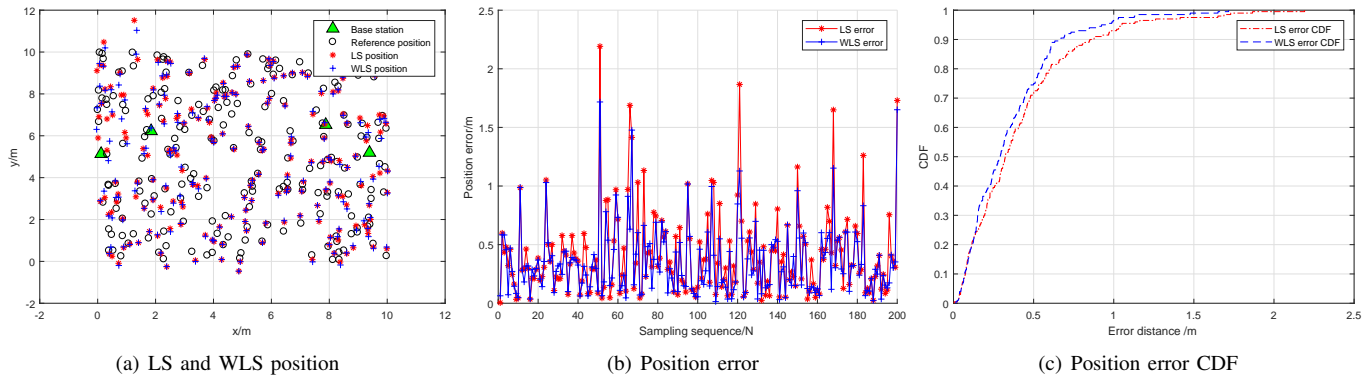


Fig. 8. The performances of LS and WLS algorithms

trajectory has oscillation and the larger the observation noise variance is, the larger the oscillation appears. It indicates that the observation noise has great influence on the measurements. However, after using the proposed EKF algorithm, the trajectory accuracy can be significantly improved and the results are much more close to the true trajectory as shown in Fig.7(b). Moreover, it can be seen that when the observation noise variance increases, the EKF trajectory keeps consistent. As shown in Fig.7(d), when the process noise variance becomes large, the carrier's motion will be the curvilinear. However, after using the proposed EKF algorithm, the trajectory accuracy can be significantly improved and the results are much more close to the true trajectory as shown in Fig.7(e). In Fig.7(c) and Fig.7(f), the Cumulative Distribution Functions (CDF) of positioning errors are illustrated. Specifically, when  $R=0.01$  and  $Q=10^{-8}$ , the maximum position error of LS algorithm is

over 31cm and the average position error is about 14cm. For the proposed EKF algorithm, the maximum position error is about only 20cm and the average position error is less than 9cm. The positioning accuracy has been improved by about 50%. When  $R=0.01$  and  $Q=10^{-4}$ , the maximum position error of LS algorithm is over 57cm and the average position error is about 18cm. However, the maximum position error is about only 22cm and the average position error is reduced to less than 10cm when the proposed EKF fusion algorithm is used. In addition, to evaluate the performance of the WLS algorithm, we randomly generate four BSs with known positions and two hundred reference points on a 10m by 10m area. We also assume that the observation distance noise is white Gaussian noise with zero mean and variance 0.01m. The simulation results in Fig.8 show that the positioning accuracy of WLS algorithm is improved compared with LS algorithm.

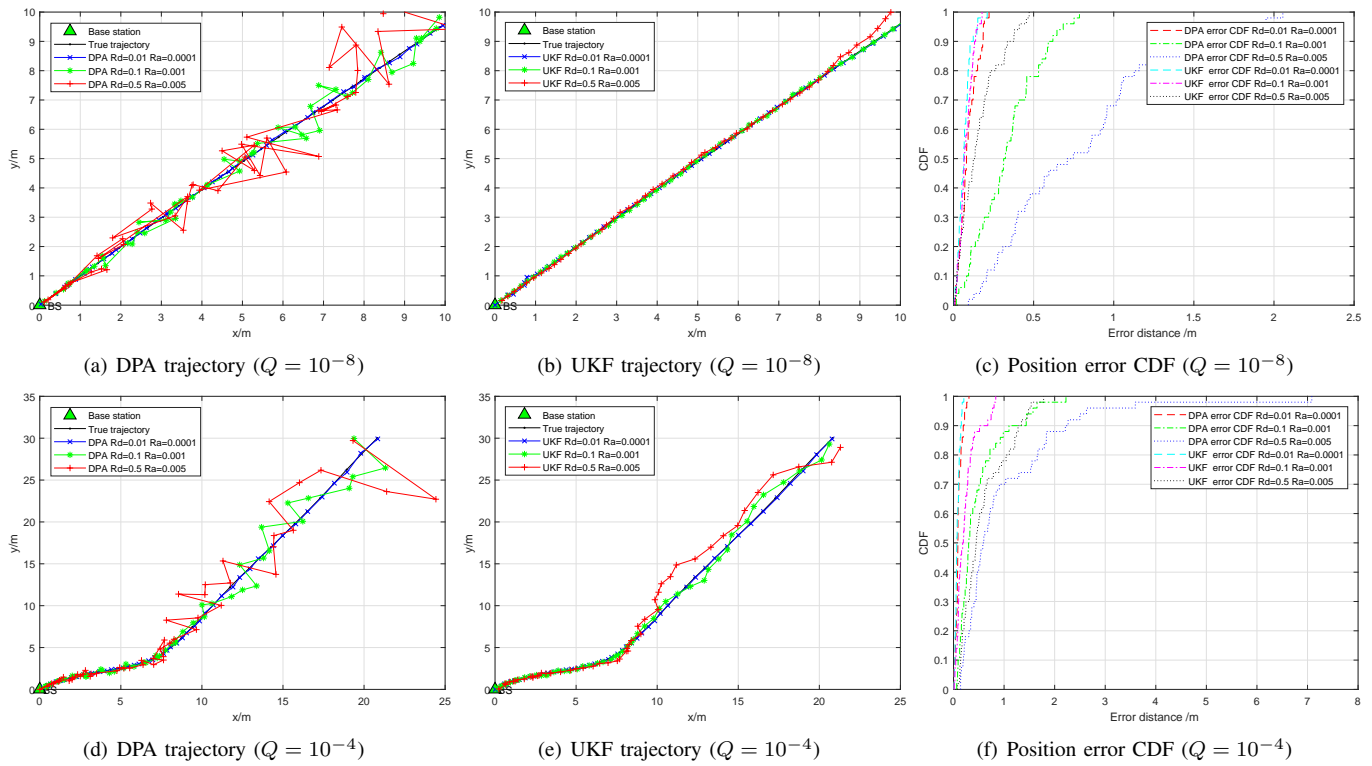


Fig. 9. The performances of DPA and UKF algorithms

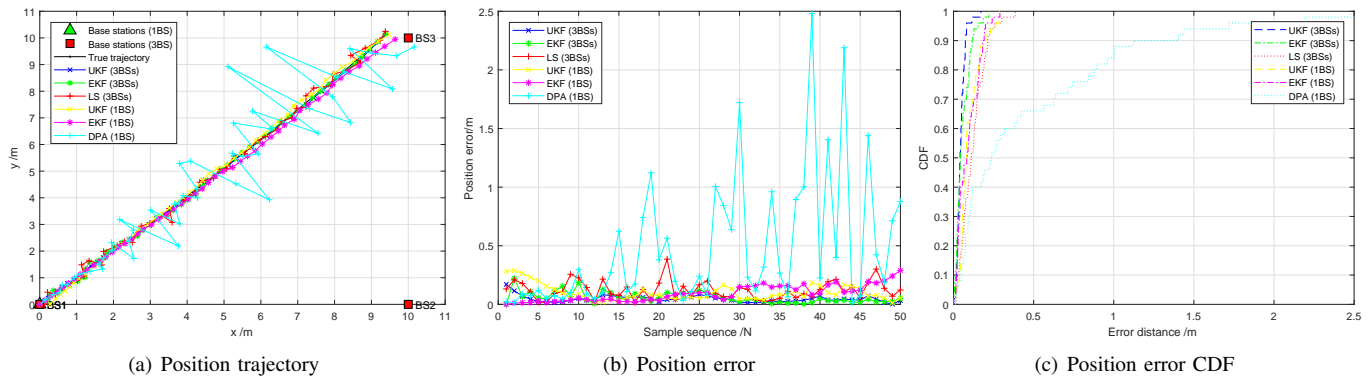


Fig. 10. The performances of EKF and UKF algorithms

### B. UKF simulation results

In the UKF simulations, it is also assumed that the tag moves in the  $xy$  plane with the initial position at  $(0,0)$ , the initial horizontal velocity and the vertical velocity are both at  $0.15\text{m/s}$ , the initial horizontal acceleration and the vertical acceleration are both at  $0.002\text{m/s}^2$ , the sample time period  $T=1\text{s}$ , and the total running time  $N=50\text{s}$ . The correlation coefficients  $\alpha=0.01$ ,  $\beta=2$ ,  $\kappa=0$  and state dimension  $n=6$ , the observation dimension  $m=2$  in UT. In the following,  $R_d$  and  $R_a$  denote the observation distance noise variance and angle noise variance, respectively.

Fig.9 compares the performances of the DPA without filtering and UKF algorithms. As shown in Fig.9(a), at the initial stage, the DPA trajectory can continuously track the true trajectory. However, after several iterations, the oscil-

lation appears. This is mainly due to the accumulation of observation angle noise. On the other hand, as shown in Fig.9(b), the UKF trajectory can still track the true trajectory, which indicates that the proposed UKF algorithm can improve the positioning accuracy based on single observation distance and angle. Moreover, it is shown that when the observation noise variance increases, the UKF trajectory is still consistent with the true trajectory. Comparing Fig.9(a) with Fig.9(d), Fig.9(b) with Fig.9(e), as the process noise becomes larger, the carrier's motion is to the curvilinear motion. In addition, the cumulative distribution function of positioning error is shown in Fig.9(c) and Fig.9(f). Specifically, when  $R_d=0.1$ ,  $R_a=0.001$  and  $Q=10^{-8}$ , the maximum position error of DPA is over  $78\text{cm}$  and the average position error is about  $33\text{cm}$ . However, for proposed UKF algorithm, the maximum position error is about only  $18\text{cm}$  and the average position error is

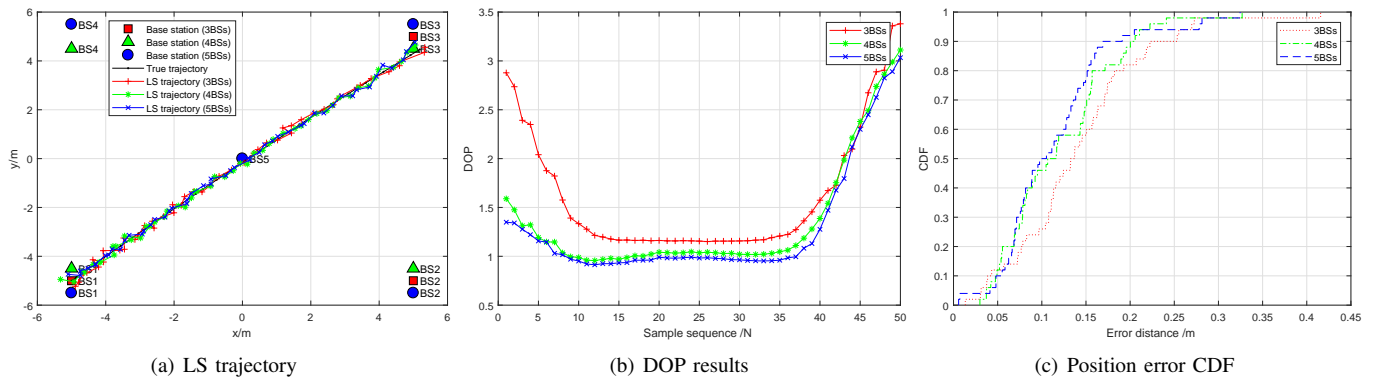


Fig. 11. The Dilution of precision

less than 7cm. The positioning accuracy has been improved by about 78%. In order to better evaluate the performances of two positioning algorithms and two filtering algorithms, we compare their performances with the same assumption  $R=0.01$ ,  $R_d=0.01$ ,  $R_a=0.01$  and  $Q=10^{-8}$ .

Fig.10 shows the results of different positioning algorithms based on single BS and three BSs. The average positioning error of LS algorithm based on three BSs is 15cm, while that of the DPA algorithm based on single BS is 53cm. The average positioning error of EKF fusion algorithm based on three BSs is 6cm, and that of single BS is 18cm. The average positioning error of UKF fusion algorithm based on three BSs is 5cm, and that of single BS is 13cm. In summary, when the positioning accuracy requirement is high, multiple BS positioning algorithm can be selected, otherwise, single BS positioning algorithm can be selected to reduce the complexity and cost of deploying BSs.

### C. DOP simulation results

In Fig.11, we evaluate the influence of the distribution of BS. In triangle model, the three BSs are located at  $(-5,-5)$ ,  $(5,-5)$  and  $(5,5)$ ; in square model, the four BSs are located at  $(-5,-4.5)$ ,  $(5,-4.5)$ ,  $(5,4.5)$  and  $(-5,4.5)$ ; in X model, the five BSs are located at  $(-5,-5.5)$ ,  $(5,-5.5)$ ,  $(5,5.5)$ ,  $(-5,5.5)$  and  $(0,0)$  as shown in Fig.11(a). In Fig.11(b), it can be seen that the HDOP value is relatively small in the center area and gradually increases outwards the edge of BSs. It is also shown that increasing the number of BSs can reduce the HDOP value. However, the effect becomes less and less and it will increase the system complexity with the increase of BSs. The CDF result of the system positioning error is shown in Fig.11(c).

### D. Experiments and results

The hardware used in this experiment is shown in Fig.12, which is with the "baseplate and module" structure. The baseplate adopts STM32F103T8U6 microcomputer as the main control chip. The peripheral circuit includes power, LED indicator, lithium battery management, LIS3DH and accelerometer, etc. The modules are configured with DWM1000 of Decawave and MAX2000 of YCHIOT. Note that the hardware can be configured as BS or tag through the USB instruction.

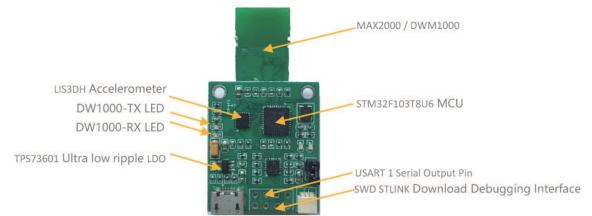
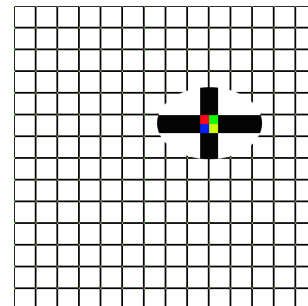


Fig. 12. Hardware architecture of positioning module

The experimental environment is shown in Fig.13(a), where each smaller grid on the ground is a square with a side length of 0.5m. To accurately measure the true position of the tag, all the brackets and the BSs are deployed in the same way. Then, the true position of the tag is determined by the vertical projection of the center points of small red, green, blue and yellow squares from the top of the module antenna to the ground grid, as shown in Fig.13(b).



(a) Experimental environment



(b) Ground grid

Fig. 13. Indoor positioning and navigation experiment

Since the actual ranging measurement is affected by the environment including latitude, longitude, air quality, obstacle height and other factors, we must first calibrate the module. Particularly, the calibration coefficients can be obtained by measuring the distance between BS and tag. There are many fitting formulas to fit the data and the simplest linear equation is used in the experiments. Obviously, the ranging accuracy will become better after calibrating as shown in Fig.14.

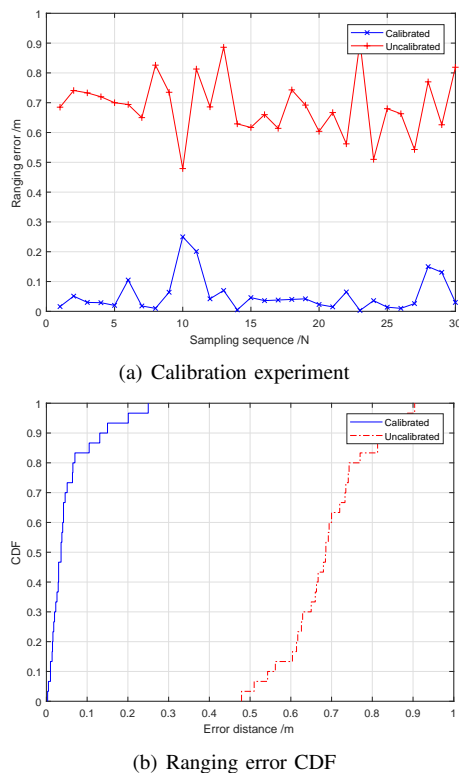


Fig. 14. Experiment of ranging calibration

In the first experiment scenario, the tag starts from (1,1) and moves two rounds along a square with a side length of 4m as shown in Fig.15. The experimental results show that the LS trajectory oscillates relative to the true trajectory due to the influence of noise. The AUAM filtering trajectory has a good tracking effect in the initial stage, but the error caused by the acceleration becomes larger with the passage of time. The AUM filtering trajectory keeps continuous tracking. It can also be seen that the positioning trajectories of AUAM and AUM algorithm are smoother than the LS algorithm.

In the second experiment scenario, the tag moves along a square with a side length of 6m as shown in Fig.16. In the spiral experiment, the results show that the root mean square error (RMSE) of  $x$  axis is 7.79cm, and that of  $y$  axis is 6.32cm. In the circuitous experiment, the results show that the RMSE of  $x$  axis is 5.50cm, and that of  $y$  axis is 5.03cm. It is because there are fewer sample points on the edge of the BSs in the circuitous experimental. Thus, when the tag is closer to the center, the positioning accuracy is better. It implies that expanding the deployment of the BSs and ensuring that the tag always moves in the center of the coverage can effectively improve the positioning accuracy.

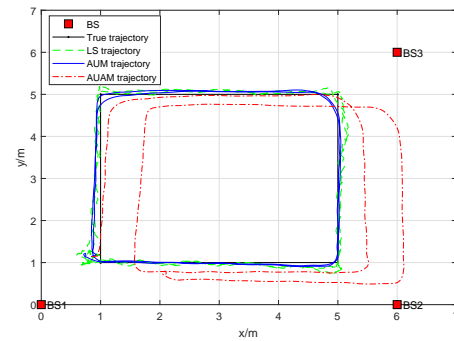
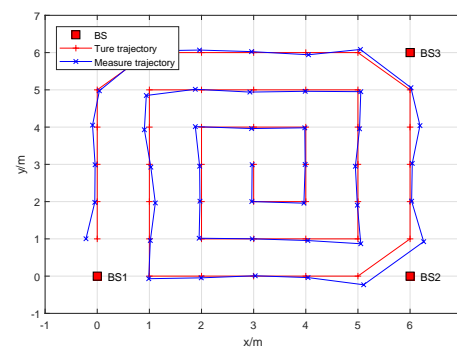
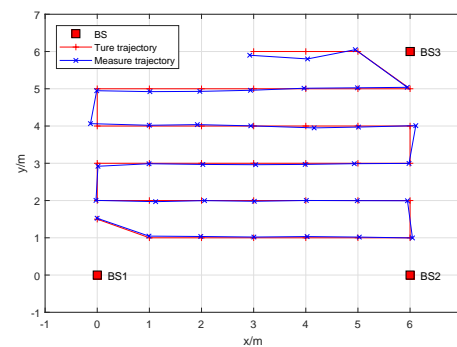


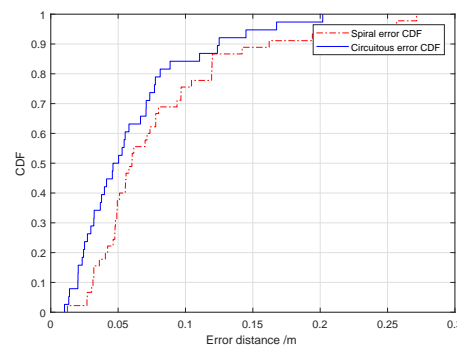
Fig. 15. Experiments of AUAM and AUM models



(a) Experiments of spiral



(b) Experiments of circuitous



(c) Position error CDF

Fig. 16. Experiments of spiral and circuitous

## V. CONCLUSION

In this paper, a fusion positioning system based on IMU and UWB are studied. The data obtained by IMU is used for the state equation of Kalman filter while the data obtained by UWB is used for the observation equation of Kalman filter. First, EKF algorithm based on multiple observation BSs is introduced to improve the positioning accuracy. Then, an efficient UKF algorithm based on single observation BS is proposed to reduce the deployment complexity of BS and lower the cost. In addition, to reduce the jitter of positioning data, two approximate motion models, namely, AUM and AUAM, are proposed to make the positioning results smoother and more stable. In addition, the experimental results show the proposed EKF algorithm improves the positioning accuracy by 54% compared to LS algorithm and the proposed UKF algorithm improves the positioning accuracy by 50% compared to DPA algorithm. Note that in our system, we have only considered the Gaussian noise distribution. Thus, for reducing the complexity, we have only studied the EKF and UKF methods. In the future work, we will consider a generalized noise distribution, and focus on the application and the optimization of other filter methods, e.g., particle filter.

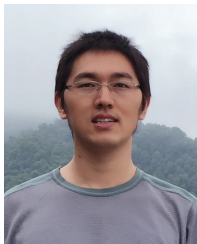
## REFERENCES

- [1] Y. Zhuang, Q. Wang, M. Shi, P. Cao, L. Qi, and J. Yang, "Low-power centimeter-level localization for indoor mobile robots based on ensemble kalman smoother using received signal strength," *IEEE Internet of Things J.*, pp. 1-1, Mar. 2019.
- [2] Y. Zhuang and N. El-Sheimy, "Tightly-coupled integration of WiFi and MEMS sensors on handheld devices for indoor pedestrian navigation," *IEEE Sensors J.*, vol. 16, no. 1, pp. 224-234, Jan. 2016.
- [3] Y. Li, Y. Zhuang, P. Zhang, H. Lan, X. Niu, and N. El-Sheimy, "An improved inertial/wifi/magnetic fusion structure for indoor navigation," *Inf. Fusion*, vol. 34, pp. 101-119, Mar. 2017.
- [4] Y. Li, Z. He, Z. Gao, Y. Zhuang, C. Shi, and N. El-Sheimy, "Toward robust crowdsourcing-based localization: a fingerprinting accuracy indicator enhanced wireless/magnetic/inertial integration approach," *IEEE Internet of Things J.*, vol. 6, no. 2, pp. 3585- 600, Apr. 2019.
- [5] Y. Zhuang, J. Yang, L. Qi, Y. Li, Y. Cao, and N. El-Sheimy, "A pervasive integration platform of low-cost MEMS sensors and wireless signals for indoor localization," *IEEE Internet of Things J.*, vol. 5, no. 6, pp. 4616-4631, Dec. 2018.
- [6] C. Ren, Q. Liu, and T. Fu, "A novel self-calibration method for MIMU," *IEEE Sensors J.*, vol. 15, no. 10, pp. 5416-5422, Oct. 2015.
- [7] K. Guo, Z. Qiu, C. Miao, A. H. Zaini, C. Chen, M. Wei, and L. Xie, "Ultra-wideband-based localization for quadcopter navigation," *Unmanned Syst.*, vol. 4, no. 1, pp. 23-24, Feb. 2016.
- [8] A. Chandra, A. Proke, T. Mikulek, J. Blumenstein, P. Kukolev, T. Zemen, and C. F. Mecklenbrucker, "Frequency-domain in-vehicle UWB channel modeling," *IEEE Trans. Veh. Technol.*, vol. 65, no. 6, pp. 3929-3940, Jun. 2016.
- [9] S. Wang, G. Mao, and J. A. Zhang, "Joint time of arrival estimation for coherent UWB ranging in multipath environment with multi user interference," *IEEE Trans. Signal Process.*, pp. 1-1, May. 2019.
- [10] A. Abdulrahman, A. S. AbdulMalik, A. Mansour, A. Ahmad, A. H. Suheer, A. A. Mai, and S. Hend, "Ultra wideband indoor positioning technologies: analysis and recent advances," *Sensors*, vol. 16, no. 5, pp. 707, May. 2016.
- [11] S. Marano, W. M. Gifford, H. Wymeersch, and M. Z. Win, "NLOS identification and mitigation for localization based on UWB experimental data," *IEEE J. Sel. Areas Commun.*, vol. 28, no. 7, pp. 1026-1035, Aug. 2010.
- [12] Y. Lu, J. Yi, L. He, X. Zhu, and P. Liu, "A hybrid fusion algorithm for integrated INS/UWB navigation and its application in vehicle platoon formation control," *Proc. Int. Conf. Comput. Sci., Electronics and Communication Eng. (CSECE)*, Feb. 2018.
- [13] M. Gunia, F. Protze, N. Joram, and F. Ellinger, "Setting up an ultra-wideband positioning system using off-the-shelf components," *Proc. IEEE 13th Workshop on Positioning Navigation and Commun. (WPNC)*, pp. 1-6, Oct. 2016.
- [14] Y. Zhuang, Y. Cao, N. El-Sheimy, and J. Yang, "Guest editorial: special issue on toward positioning, navigation, and location-based services (pnlbs) for internet of things," *IEEE Internet of Things J.*, vol. 5, no. 6, pp. 4613-4615, Dec. 2018.
- [15] L. Yao, Y.-W. A. Wu, L. Yao, and Z. Liao, "An integrated IMU and UWB sensor based indoor positioning system," *Proc. IEEE Int. Conf. on Indoor Positioning and Indoor Navigation (IPIN)*, pp. 1-8, Sep. 2017.
- [16] Y. Zhong, T. Liu, B. Li, L. Yang, and L. Lou, "Integration of UWB and IMU for precise and continuous indoor positioning," *Proc. IEEE Ubiquitous Positioning, Indoor Navigation and Location-Based Services (UPINLBS)*, pp. 1-5, Mar. 2018.
- [17] P. K. Yoon, S. Zihajehzadeh, B.-S. Kang, and E. J. Park, "Robust biomechanical model-based 3-D indoor localization and tracking method using UWB and IMU," *IEEE Sensors J.*, vol. 17, no. 4, pp. 1084-1096, Feb. 2017.
- [18] S. Zihajehzadeh and E. J. Park, "A novel biomechanical model-aided IMU/UWB fusion for magnetometer-free lower body motion capture," *IEEE Trans. Syst., Man, and Cybern. Syst.*, vol. 47, no. 6, pp. 927-938, Jun. 2017.
- [19] S. Zihajehzadeh, P. K. Yoon, B. S. Kang, and E. J. Park, "UWB-aided inertial motion capture for lower body 3-D dynamic activity and trajectory tracking," *IEEE Trans. Instrum. and Meas.*, vol. 64, no. 12, pp. 3577-3587, Dec. 2015.
- [20] T. Seel and S. Ruppert, "Eliminating the effect of magnetic disturbances on the inclination estimates of inertial sensors," in *Proc. 20th IFAC World Congress*, vol. 50, no. 1, pp. 8798-8803, Jul. 2017.
- [21] L. Chang, J. Li, and S. Chen, "Initial alignment by attitude estimation for strapdown inertial navigation systems,"



*IEEE Trans. Instrum. and Meas.*, vol. 64, no. 3, pp. 784-994, Mar. 2015.

- [22] G. Wang, S. Qian, Q. Lv, H. Wei, H. Lin, and B. Liang, "UWB and IMU system fusion for indoor navigation," *Proc. IEEE 37th Chinese Control Conf. (CCC)*, pp. 4946-4950, Jul. 2018.
- [23] A. Wang and Y. Song, "Improved SDS-TWR ranging technology in UWB positioning," *Proc. IEEE Int. Conf. Sensor Netw. and Signal Process. (SNSP)*, pp. 222-225, Oct. 2018.
- [24] A. Noureldin, T. B. Karamat, M. D. Eberts, and A. El-Shafie, "Performance enhancement of MEMS-based INS/GPS integration for low-cost navigation applications," *IEEE Trans. Veh. Technol.*, vol. 58, no. 3, pp. 1077-1096, Mar. 2009.
- [25] Y. Zhuang, Y. Li, L. Qi, H. Lan, J. Yang, and N. El-Sheimy, "A two-filter integration of MEMS sensors and WiFi fingerprinting for indoor positioning," *IEEE Sensors J.*, vol. 16, no. 13, pp. 5125-5126, Jul. 2016.
- [26] S. Wang, Y. Lyu, and W. Ren, "Unscented transformation based distributed nonlinear state estimation: algorithm, analysis, and experiments," *IEEE Trans. Control Syst. Technol.*, pp. 1-14, Jul. 2018.
- [27] E. A. Wan and R. Van Der Merwe, "The unscented Kalman filter for nonlinear estimation," *Proc. IEEE Adaptive Syst. for Signal Process., Commun., and Control Symp. (ASSPCC)*, pp. 153-158, Oct. 2000.
- [28] C. Tang, X. Hu, S. Zhou, R. Guo, F. He and L. Liu, "Improvement of orbit determination accuracy for beidou navigation satellite system with two-way satellite time frequency transfer," *Advances in Space Research*, vol. 58, pp. 1390-1400, May. 2016



**Daquan Feng** received his Ph.D. degrees in Information Engineering from the National Key Laboratory of Science and Technology on Communications, University of Electronic Science and Technology of China, Chengdu, China in 2015. He had been a visiting student in the School of Electrical and Computer Engineering, Georgia Institute of Technology, USA, from 2011 to 2014. After graduation, he was a research staff in the State Radio Monitoring Center, Beijing, China, and then a Postdoctoral Research Fellow in Singapore University of Technology and

Design. He is now an assistant professor with the Guangdong Province Engineering Laboratory for Digital Creative Technology and Guangdong Key Laboratory of Intelligent Information Processing, College of Electronics and Information Engineering, Shenzhen University, Shenzhen, China. His research interests include URLLC communications, LTE-U, and massive IoT networks. He is an Associate Editor of the IEEE Communications Letters and IEEE Access.



**Chunqi Wang** is a Master student of Information and Communication Engineering with the Guangdong Province Engineering Laboratory for Digital Creative Technology and Guangdong Key Laboratory of Intelligent Information Processing, College of Electronics and Information Engineering, Shenzhen University, Shenzhen, China. He received his B.S. degree of Opto-Electronics Information Science and Engineering from the College of Testing and Opto-Electronic Engineering, Nanchang Hangkong University, Nanchang, China in 2017. His current

research interests include pedestrians and robots positioning and navigation.



**Chunlong He** received the M.S. degree in communication and information science from Southwest Jiaotong University, Chengdu, China, in 2010 and the Ph.D. degree from Southeast University, Nanjing, China, in 2014. From September 2012 to September 2014, he was a Visiting Student with the School of Electrical and Computer Engineering, Georgia Institute of Technology, Atlanta, GA, USA. Since 2015, he has been with the College of Electronics and Information Engineering, Shenzhen University, where he is currently an Associate Professor. His

research interests include communication and signal processing, green communication systems, channel estimation algorithms, and limited feedback techniques. Dr. He is a member of the Institute of Electronics, Information, and Communication Engineering. He is currently an Associate Editor of IEEE Access.



**Yuan Zhuang** (M'16) received the bachelor degree in information engineering from Southeast University, Nanjing, China, in 2008, the master degree in microelectronics and solid-state electronics from Southeast University, Nanjing, China, in 2011, and the Ph.D. degree in geomatics engineering from the University of Calgary, Canada, in 2015. He was Algorithm Designer at Trusted Positioning Inc., Canada; Lead Scientist at Bluvision Inc., USA; and has been Professor at State Key Laboratory of Information Engineering in Surveying, Mapping and

Remote Sensing, Wuhan University, China. His current research interests include multi-sensors integration, real-time location system, personal navigation system, wireless positioning, Internet of Things (IoT), and machine learning for navigation applications. To date, he has co-authored over 50 academic papers and 11 patents and has received over 10 academic awards. He is an associate editor of IEEE Access, the guest editor of the IEEE Internet of Things Journal and IEEE Access, and a reviewer of over 10 IEEE journals.



**Xiang-Gen Xia** (M'97, S'00, F'09) received his B.S. degree in mathematics from Nanjing Normal University, Nanjing, China, and his M.S. degree in mathematics from Nankai University, Tianjin, China, and his Ph.D. degree in electrical engineering from the University of Southern California, Los Angeles, in 1983, 1986, and 1992, respectively.

He was a Senior/Research Staff Member at Hughes Research Laboratories, Malibu, California, during 1995-1996. In September 1996, he joined the Department of Electrical and Computer Engineering,

University of Delaware, Newark, Delaware, where he is the Charles Black Evans Professor. His current research interests include space-time coding, MIMO and OFDM systems, digital signal processing, and SAR and ISAR imaging. Dr. Xia is the author of the book *Modulated Coding for Intersymbol Interference Channels* (New York, Marcel Dekker, 2000).

Dr. Xia received the National Science Foundation (NSF) Faculty Early Career Development (CAREER) Program Award in 1997, the Office of Naval Research (ONR) Young Investigator Award in 1998, and the Outstanding Overseas Young Investigator Award from the National Nature Science Foundation of China in 2001. He is currently serving and has served as an Associate Editor for numerous international journals including IEEE Wireless Communications Letters, IEEE Transactions on Signal Processing, IEEE Transactions on Wireless Communications, IEEE Transactions on Mobile Computing, and IEEE Transactions on Vehicular Technology. Dr. Xia is Technical Program Chair of the Signal Processing Symp., Globecom 2007 in Washington D.C. and the General Co-Chair of ICASSP 2005 in Philadelphia.